A Global View of Swell and Wind Sea Climate in the Ocean by Satellite Altimeter and Scatterometer

GE CHEN

Ocean Remote Sensing Institute, Ocean University of Qingdao, Qingdao, China

BERTRAND CHAPRON AND ROBERT EZRATY

Département d'Océanographie Spatiale, Centre de Brest, IFREMER, Plouzane, France

DOUGLAS VANDEMARK

Wallops Flight Facility, NASA Goddard Space Flight Center, Wallops Island, Virginia

(Manuscript received 8 August 2001, in final form 18 February 2002)

ABSTRACT

Numerous case reports and regional studies on swell and wind sea events have been documented during the past century. The global picture of these common oceanic phenomena, however, is still incomplete in many aspects. This paper presents a feasibility study of using collocated wind speed and significant wave height measurements from simultaneous satellite scatterometer and altimeter sources to observe the spatial and seasonal pattern of dominant swell and wind wave zones in the world's oceans. Two energy-related normalized indices are proposed, on the basis of which global statistics of swell/wind sea probabilities and intensities are obtained. It is found that three well-defined tongue-shaped zones of swell dominance, termed ''swell pools,'' are located in the eastern tropical areas of the Pacific, the Atlantic, and the Indian Oceans, respectively. Regions of intensive wave growth are observed in the northwest Pacific, the northwest Atlantic, the Southern Ocean, and the Mediterranean Sea. Seasonality is distinct for the climate of both swell and wind sea, notably the large-scale northward bending of the swell pools in boreal summer, and the dramatic shift of wave-growing extent from a summer low to an autumn high. The results of this study may serve as a useful reference for a variety of activities, such as ocean wave modeling, satellite algorithm validation, coastal engineering, and ship routing, when information on swell and wind sea conditions is needed.

1. Introduction

Waves are one of the most fundamental and ubiquitous phenomena present at the air–sea interface. Since the spectrum of ocean waves is continuous and infinite, they are likely to cover a wide range of frequency and wavelength. The dominant portion of the wave spectrum in terms of energy is known to be associated with gravity waves whose period ranges from 1 to 30 s [see, e.g., Figs. 1.2–1 of Kinsman (1965)]. Therefore it comes as no surprise that a majority of ocean wave studies are devoted to gravity waves.

Two main classes of gravity waves exist in the ocean, namely, the so-called wind wave (or wind sea when emphasizing its state) and swell. The former refers to young waves under growth or in equilibrium with local wind, while the latter is defined as waves generated elsewhere and propagating over large distances. As a rule of thumb, a period of 10 s may be taken as separating swell from wind wave (Kinsman 1965). Because of the different dynamics involved, studies on swell and wind wave usually have different motivations and concerns. Swell is of increasing concern because of its potentially destructive consequences on coastal structures and sea-going activities (Mettlach et al. 1994). For example, in October 1987 nine elementary school children were drowned by the sudden arrival of a typhoon-generated swell hitting the Mau-Pi-Tou coast of Taiwan (Liang 1990). On the other hand, wind wave with a fetch up to an equilibrium state is of particular importance for the development and verification of wave models. Many previous studies, both theoretical and experimental, have been carried out in this regard (e.g., Pierson and Moskowitz 1964; Hasselmann et al. 1973; Hasselmann et al. 1988; Kahma 1981; Ewing and Laing 1987; Ebuchi et al. 1992).

In view of the different natures and impacts of swell and wind sea, a global knowledge of each individual

Corresponding author address: Dr. Ge Chen, Ocean Remote Sensing Institute, Ocean University of Qingdao, 5 Yushan Road, Qingdao 266003, China.
E-mail: gechen@public.qd.sd.cn

process in terms of its frequency of occurrence and associated energy is highly desirable. This can be quickly understood by examining the prerequisites of the two categories of studies outlined above. Analysis of swell energy and prediction of its propagation would obviously benefit from a zero-wind condition. On the other hand, a wind-wave-related investigation always seeks an ideal sea state with no swell presence, especially when time and site have to be determined or selected for a field experiment. Despite their different dynamics, swell and wind sea often overlap in wave characteristics. Moreover, they are usually a complex mixture at a given location. This sometimes makes it difficult to separate the two phenomena in real observations. In this study, taking the advantage of the newly available simultaneous measurements from National Aeronautics and Space Administration (NASA) satellite sensors, the TOPEX altimeter and the NSCAT and QuikSCAT (hereinafter abbreviated as QSCAT) scatterometers, an energy-based scheme is proposed to estimate the respective degree of swell and wind wave for each collocation site (section 2), on the basis of which global maps of swell and wind sea climate are produced and analyzed (sections 3 and 4). Finally, major swell and wind wave zones in the world's oceans are discussed and summarized (section 5).

2. Data and scheme

a. Wind–wave relation

According to wave forecasting models, sea surface wind speed and significant wave height follow a monotonical relationship under a growing sea up to the fully developed stage. This final stage is usually reached when the phase velocity corresponding to the dominant peak wave slightly exceeds the wind speed. The significant wave heights for fully developed seas were proposed by various authors, for example, Sverdrup and Munk (1947), Neumann (see Kinsman 1965), Pierson and Moskowitz (1964), Ewing and Laing (1987), and Hasselmann et al. (1988). Among these relationships, the Wave Model (WAM)-derived expression is found to have an intermediate overall growth rate for wind speed ranging from 0 to 30 m s^{-1} (see Pierson 1991), and is therefore chosen for our analysis.

Based on the WAM model (Hasselmann et al. 1988), the wind–wave relation for fully developed seas can be expressed as

$$H = 1.614 \times 10^{-2} U^2 \quad (0 \le U \le 7.5 \text{ m s}^{-1}) \tag{1a}$$

$$H = 10^{-2} U^2 + 8.134 \times 10^{-4} U^3 \quad (7.5 \text{ m s}^{-1} < U \le 50 \text{ m s}^{-1}), \tag{1b}$$

where U (in m s^{-1}) is the wind speed at 10-m height, and H (in m) is the significant wave height (Pierson 1991). A graphic illustration of Eq. (1) is shown in Fig. 1 (the thick curve), along with coincident measurements of wind speed from NSCAT/QSCAT and significant wave height from TOPEX (see section 2b). The Pierson and Moskowitz (1964) and the Ewing and Laing (1987) wind–wave relations are also included in Fig. 1 for reference. A direct implication of this graph is that the fully developed relationship may be used as a dividing line for sea state maturity: Measurements lying below the curve are mostly from a growing sea, while those above the curve are probably swell dominated. Of course this inference is not supposed to be valid in an absolute sense due to the complexity of the wind wave–swell coupling. But it is expected to give a meaningful classification of the two regimes from a statistical point of view.

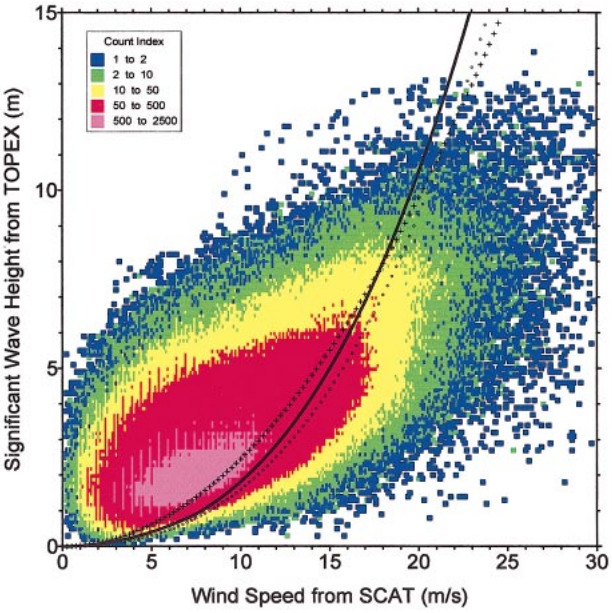

FIG. 1. A scatter diagram of sea surface wind speed and significant wave height based on the collocated TOPEX/NSCAT and TOPEX/QSCAT datasets. The wind speeds are extracted from NSCAT and QSCAT, and the significant wave heights are extracted from TOPEX. The color legend depicts data density. Also overlaid are the theoretical relations between wind speed and significant wave height for fully developed seas according to Hasselmann et al. (1988) (the WAM model), Pierson and Moskowitz (1964), and Ewing and Laing (1987), as depicted by the solid line, the crosses, and the circles, respectively.

b. Collocation dataset

With the above understanding, it is apparent that, if measurements of U and H for a given location and a given time are available with reasonable accuracy, an estimate of the swell or wind sea extent will be practically possible. A potential source of data for such an estimation is from satellite altimeters, which provide coincident measurements of U and H at nadir. However, accumulating evidence suggests that altimeter wind speed measurements can be considerably affected by long waves or swells, which are not directly coupled

TABLE 1. Some details of the TOPEX/NSCAT and TOPEX/QSCAT collocation datasets. (Duration time: mm/dd/yy.)

Collocation dataset	TOPEX/NSCAT	TOPEX/QSCAT
Duration	9/15/1996–6/30/1997	7/20/1999–3/19/2001
Spatial coverage	66°S–66°N	66°S–66°N
Number of data pairs	97 613	1 639 075
Time window	60 min	30 min
Space window	12 km	15 km

with the local wind field (Glazman and Pilorz 1990; Lefevre et al. 1994; Hwang et al. 1998; Gourrion et al. 2000). This situation violates the assumption that the radar cross section (σ_0) measured by an altimeter is purely a reflection of the short wave roughness due to local wind action, which therefore may cause systematic errors in altimeter derived wind speed.

An alternative option is to use the coincident U and H measurements from an independent scatterometer and altimeter, respectively. Differing from the specular reflection theory on which altimeter wind retrieval is based, scatterometer wind speed measurement should be, in principle, less affected by sea state because of its dominant Bragg resonant scattering mechanism (Quilfen et al. 1999). Taking the advantage of the concurrent TOPEX/NSCAT and TOPEX/QSCAT missions, a global collocation dataset of wind speed and significant wave height has been compiled (Gourrion et al. 2000, see Table 1 for a summary). Since there is still some evidence indicating that near-incidence scatterometer winds are also affected by sea state (Queffeulou et al. 1999), the crossover points where the NSCAT midbeam antenna has an incidence angle less than 40° were eliminated from our dataset. Spatial density of satellite crossover points used in this study is shown in Fig. 2. The number of collocation data within a $1° \times 1°$ cell varies from 40 to 180 with a general trend of poleward increase. A scatter diagram of the coincident U and H from the collocation dataset is shown in Fig. 1. The color legend depicts data density. It is apparent that a large majority of the data points are above the theoretical U–H line, which corresponds to a mature sea state, implying a systematic swell existence in the world's oceans. Figure 1 also suggests, however, that the possibility of encountering an underdeveloped sea increases rapidly with wind speed beyond 10 m s^{-1}. It is almost impossible to reach the fully developed stage in the real ocean when the wind speed is greater than 20 m s^{-1}.

c. Swell and wind sea indices

In order to quantify the frequency of swell and wind wave occurrences, two probability indices are introduced

$$P_s = N_s/N \tag{2a}$$

$$P_w = N_w/N, \tag{2b}$$

where N_s and N_w are the number of swell and wind wave events at a given crossover point, respectively. Note that $N = N_s + N_w$, thus $P_s + P_w = 1$. This means that, in a relative sense, any true sea state is considered as either swell dominated (cases above the fully developed wind–wave curve in Fig. 1) or wind sea dominated (cases below the fully developed wind–wave curve in Fig. 1). Obviously, the values of P_s and P_w vary geographically and seasonally.

Next, we assume that the total wave energy [i.e., altimeter observed energy, E_o, in the case of swell, and theoretically predicted energy, E_p, in the case of wind sea, see Eqs. (3) and (6) below] consists of two parts: swell-associated energy (E_s) and wind-wave-associated energy (E_w). For swell cases above the fully developed

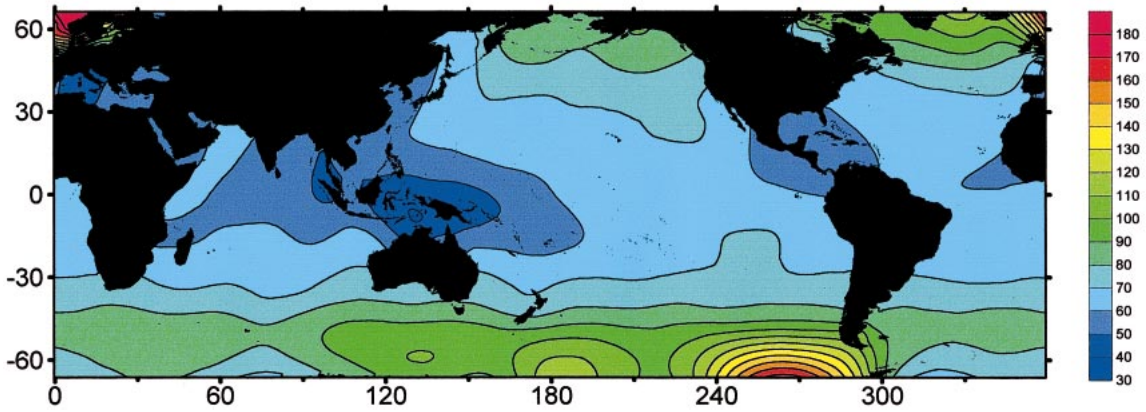

FIG. 2. Geographical distribution of the spatial density of satellite crossover points used in this study.

curve in Fig. 1, the degree of swell dominance can be estimated through the following normalized index:

$$S = \frac{E_s}{E_o} = \frac{E_o - E_w}{E_o} = \frac{E_o - E_p \times P_w}{E_o}. \quad (3)$$

Statistically, wind-wave-related energy (E_w) can be approximated as the product of the predicted energy [according to the observed wind speed, see Eq. (5) below], E_p [or the observed energy, E_o, in the case of wind sea, see Eq. (6) below], and the wind sea probability, P_w. The inclusion of P_w is based on the understanding that, in the real ocean, cases of mature wind seas are rare. It serves as a reduction factor that varies from 0 to 1 in space and time. By introducing P_w we assume that, statistically, the extent of premature wave development is proportional to the wind sea probability at a given location. The validity of this approximation can be understood by considering the two extreme cases. If $P_w = 0$, there will be no wind wave occurrence, hence, no wind-sea-related energy; if $P_w = 1$, there will be a permanent wind wave existence, which implies a trend of approaching the fully developed stage in the end. It is understood that wave energy is related to significant wave height by

$$H^2 = 16E. \quad (4)$$

Thus, Eq. (3) becomes

$$S = 1.0 - \left[\frac{H_p(U_{\text{scat}})}{H_{\text{alt}}}\right]^2 P_w, \quad (5)$$

where H_{alt} is the altimeter-measured significant wave height, and H_p is the fully developed wave height, which can be determined through Eq. (1) by using scatterometer wind speed, U_{scat}.

Knowing that measurements lying below the fully developed curve in Fig. 1 correspond to wind seas, their ''growing potential'' can be estimated through a normalized energy index defined as

$$W = \frac{E_p - E_w}{E_p} = \frac{E_p - E_o \times P_w}{E_p}. \quad (6)$$

Following similar procedures as for the swell index, we have

$$W = 1.0 - \left[\frac{H_{\text{alt}}}{H_p(U_{\text{scat}})}\right]^2 P_w. \quad (7)$$

Based on Eqs. (5) and (7), the two energy indices can be estimated for each collocated point. In principle, S and W can vary from 0 to 1 with U_{scat}, H_{alt}, and P_w. In the extreme case of a pure swell ($U_{\text{scat}} = 0$, $H_{\text{alt}} > 0$) or a pure wind sea at its very beginning ($U_{\text{scat}} > 0$, $H_{\text{alt}} = 0$), we have $S = 1$ and $W = 1$, respectively. While in the ideal case of a pure fully developed sea [U_{scat} and H_{alt} satisfying Eq. (1)], we have $S = 0$ and $W = 0$.

3. Swell climate

Global climatologies of swell (and wind sea) have been previously constructed in terms of wave height and direction, peak and mean wave period, as well as wave spectrum using both satellite data and model predictions (e.g., Heimbach et al. 1998; Young 1999; Heimbach and Hasselmann 2000). In this section, we examine the annual and seasonal behaviors of the swell probability and swell index as defined by Eqs. (2a) and (5), respectively. Comparisons are made between the ''physical parameter'' based climatologies produced by previous authors and the ''probability and index'' based climatologies obtained in this study. We start with a general view of the overall P_s distribution, followed by a detailed inspection of the seasonal variations of the swell index. As the effect of P_s is included in Eq. (5), the S index (and the W index in section 4) is considered to be a more comprehensive representation of the swell (wind sea) conditions. With this in mind, examinations on the seasonal changes of the simple swell frequency, P_s, (and P_w in section 4) are not presented in order to save space.

a. Swell probability

Following the scheme proposed in section 2, we first calculate the global swell probability as shown in Fig. 3a. The significant wave height climatology derived from the collocation dataset is also shown in Fig. 3b for reference. Surprisingly to some extent, P_s is found to be greater than 80% for most areas of the world's oceans. Dominant features in Fig. 3a are the three well-defined swell zones located in the tropical and subtropical areas near the east coast of each basin. These major swell zones, which we call swell pools, all have a probability value of more than 95%. Among them, the Pacific swell pool is the largest in area and highest in probability. An immediate conclusion that can be drawn from Fig. 3a is that the west coast of each continent in its low and midlatitude region is most likely to suffer from swell-caused damages. Another impressive aspect of Fig. 3a is that the geographical pattern of swell probability is of little similarity to that of the wave or wind speed climatology [see Fig. 3b and Fig. 1 of Chen et al. (2002)]. There is, however, a clear relevance to the global wind direction [see Fig. 1f of Young (1999)] in midlatitude storms where the swell is generated, followed by the turning of swell to follow a Great Circle as it propagates. As mentioned earlier, there are several other choices of the wind–wave relation in addition to the WAM-based expression in Eq. (1). The Pierson and Moskowitz (1964) model was also used to produce a similar plot of Fig. 2a (not shown). It was found that the qualitative results remain almost unchanged. Therefore, the WAM model employed here is likely to be representative for our purpose.

The seasonal variations of global and hemispherical

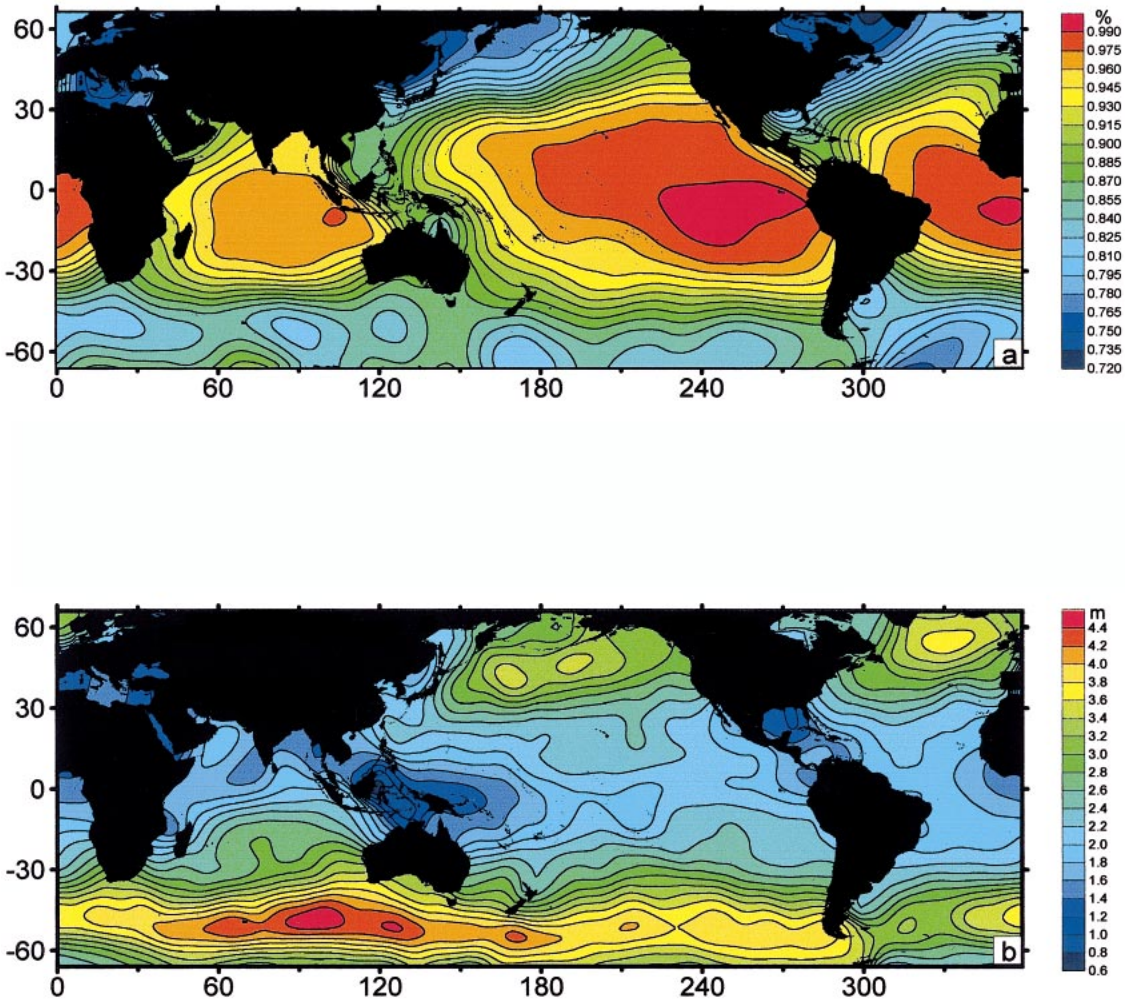

FIG. 3. Global distributions of (a) swell probability and (b) significant wave height derived from the collocated TOPEX/NSCAT and TOPEX/QSCAT datasets.

swell probability are presented in Table 2 (season in this paper refers to the Northern Hemisphere unless otherwise specified). It can be seen that the swell occurrence undergoes a contrary annual cycle for the two hemispheres. In the Northern Hemisphere P_s reaches a maximum in summer and a minimum in winter. An opposite cycle is observed for the Southern Hemisphere. Note that P_s is anticorrelated with wind speed in both hemispheres. These seem to suggest that swell pools get their swells mostly from the winter hemisphere. The seasonality of the globally averaged swell probability is insignificant as a result of the cancellation effect of the two phase-opposite hemispheric variations. However, a weak peak can still be identified in spring, followed by a relative low in summer.

TABLE 2. Seasonal variations of global and hemispherical swell probability.

Season (Months)	Swell probability (%)				
	Spring (MAM)	Summer (JJA)	Autumn (SON)	Winter (DJF)	Total
N. Hemisphere	90.5	92.3	89.8	85.5	89.1
S. Hemisphere	88.5	85.8	87.7	90.1	88.4
Global	89.2	88.0	88.4	88.8	88.7

It is somewhat difficult to find quantitative results on swell (or wind sea) probability from previous studies that can be directly compared to Fig. 3a (and those appearing in the following sections). However, there are indeed some general descriptions that can be used as qualitative references. In his well-known book on wind waves, Kinsman (1965) pointed out that ''swell from winter storms in high latitudes, both north and south, commonly reaches the equatorial region.'' In another book by Groen (1967), it was indicated that ''there is always a swell on the oceans of the world, somewhat more so here, a little less there. The waves of a swell are certainly well traveled, for they visit places thou-

sands of miles from the area of their origin. As they are particularly conspicuous in districts where there is commonly little wind, these are the best-known places for a big swell.'' These early descriptions are generally consistent with what we have seen in Fig. 3a. They are correct in tracking the swell zones down to the tropical oceans, but fail to predict their east preference.

Some regional swell observations also exist in the literature that can be related to our results. More than half a century ago, Barber and Ursell (1948), and Munk and Snodgrass (1957) indicated the ability of a swell to travel over very large distances across ocean basins. During the austral winter of 1963, the first major ocean wave experiment was carried out to measure the propagation of a swell across the Pacific Ocean (Snodgrass et al. 1966). Their main finding was that a long wavelength swell, once the nonlinear wave–wave interactions had become negligible, propagated without detectable attenuation beyond the immediate vicinity of the generation region. These early observations already suggested that a global view of swell statistics is needed in order to better understand their generation and propagation. As far as swell probability is concerned, Kinsman (1965) gave an example in the subtropical ocean. Based on wave observations made from January 1943 to April 1945 near Morocco, he found that Casablanca and Rabat received swell from storms between Ireland and Iceland regularly on a daily basis, which seems to be in agreement with the approximately 90%–95% swell probability of those regions as inferred from Fig. 3a. Through the analysis of historical wave records and their own measurements made near the Saint Helena Island (15.9°S, 5.7°W) during 1969–70, Cartwright et al. (1977) pointed out that it is probable that gales from the southwestern Atlantic provide background swells at all times of the year. As expected, a very high swell probability of more than 98% is found in the vicinity of the island (Fig. 3a). More recently, Forget et al. (1995) used a time series of *ERS-1* Synthetic Aperture Radar (SAR) data to monitor swell activities near the Banc d'Arguin off the Mauritanian coast. This area is located around (20.25°N, 17°W) where, according to Fig. 3a, the swell probability is between 96% and 97%. In fact, Forget et al. (1995) found swells on all the radar images used in their study for the period November 1992 through January 1993. These examples suggest that our swell probability map in Fig. 3a could be useful in a quantitative sense.

A more comparable result to Fig. 3a can be found in a recent systematic study on wave climate by Young (1999). In his work, global maps of monthly averaged peak wave period (T_p) and wave direction (θ_w) were constructed for a 5-yr period from June 1992 to May 1996 using the European Centre for Medium-Range Weather Forecasts (ECMWF) wave products based on the WAM model. Considering T_p as a reliable proxy of long period waves, he attributed the consistently rougher wave climate off the west coasts of the Americas as well as Australia [see Fig. 1c of Young (1999)] to swells originally generated in the intense wave region of the Southern Ocean between Australia and South Africa. The dominance of large T_p on the west coasts, though less well defined compared to our P_s map, provides direct support for the swell pools identified in Fig. 3a. It should be noted, however, the swell zone in the Atlantic Ocean appears to be much weaker compared to the Pacific and Indian Oceans on Young's T_p map, in contrast to the equally well defined swell zones in the three ocean basins revealed by our result. Also, it needs to be recognized that the T_p distribution [Fig. 1a of Young (1999)] is much more correlated to wave climate [see Fig. 1c of Young (1999) or our Fig. 3b] than our P_s distribution (Fig. 3a), implying that the peak wave period reflects a mixture of swell and long-period wind wave. In other words, P_s could be a more effective and independent parameter in characterizing the swell pattern compared to T_p.

b. Swell index

Knowing the swell probability P_s (hence P_w), the swell intensity index, S, can be calculated through Eq. (5). Figure 4 shows the globally averaged S distributions for the four seasons. These maps retain the basic features of Fig. 3a but reveal more regional details on seasonal basis. The most striking feature is the northward bending of the tongue-shaped swell pools in the Pacific and the Atlantic Oceans during summer time (Fig. 4b). The scale of the bending is remarkable: The tips of the swell ''tongues'' shift up to 50°–60°N in summer from their normal positions at 10°–15°N during the rest of the year. This may indicate a systematic northward propagation of strong swells generated by storms in the Southern Hemisphere during the austral winter. It is understood that in all parts of the Southern Ocean, families of very large swells (8–10 m in H) are frequently generated by strong atmospheric storm systems (Hamilton 1992). Such storm systems are known to have a significant austral winter enhancement. Based on the analysis of seasonal maps of wave direction (θ_w) derived from the WAM model, Young (1999) observed a ''front'' in the Pacific Ocean, which marks the boundary of swells from the two hemispheres (see his Fig. 1e). This front is located between New Zealand and Central America in January, and moves northward to lie between Mexico and New Guinea in April. By July the front has almost completely disappeared, as a result of the full occupation of the Southern Ocean swell system in the entire North Pacific. In October, the swell front shifts back to the equator in response to the strengthening of the North Pacific wave field. This process agrees well with the observed annual migration of the swell pool in the Pacific Ocean, as shown in Fig. 4. Again, the model-based θ_w field fails to produce a similar annual cycle for the Atlantic swell pool, which is equally distinct in Fig. 4.

The summer feature of the swell pools discussed

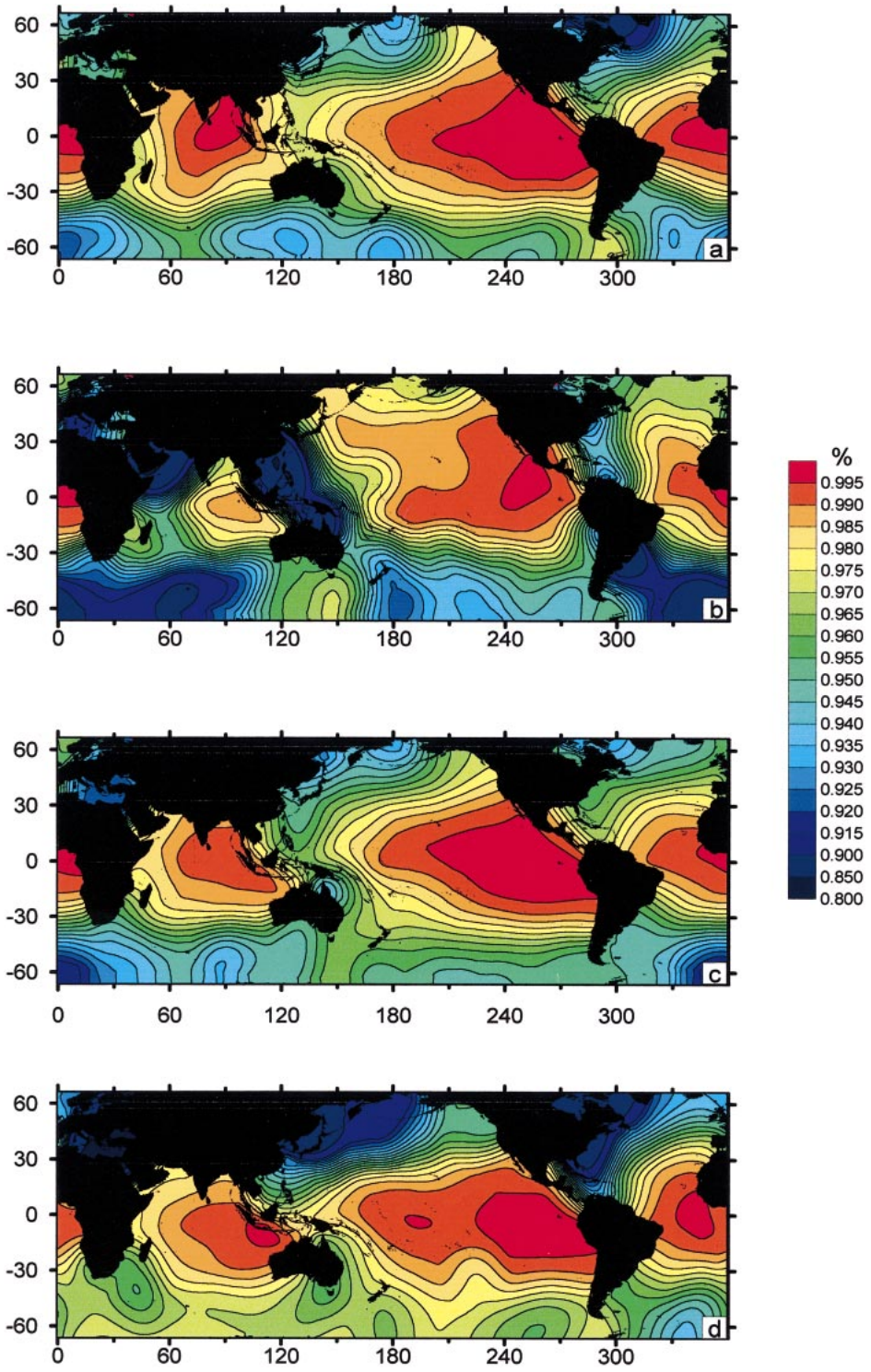

FIG. 4. Global distributions of the swell index for (a) spring (MAM), (b) summer (JJA), (c) autumn (SON), and (d) winter (DJF), derived from the collocated TOPEX/NSCAT and TOPEX/QSCAT datasets.

above is also consistent with available field or space observations. Groen (1967) described the arrival of swells at the British coast from the Southern Hemisphere in summer when the ocean is very calm. Based on Seasat altimeter data that cover the full summer of 1978, Mognard (1984) was able to track the trajectories of a number of swell events in the South Pacific. These swells, generated in the areas south of 40°S, are found to propagate systematically northward. Moreover, the finding that the swell families originated from the Ross Sea neighborhood impinge upon the coasts of North America with much greater energy than those from south of Australia corresponds well to the eastern intensification of our swell index (Fig. 4). Using 19 data buoys in the western North Atlantic around (35°N, 65°W), Hamilton (1992) reported a long-period, low-amplitude swell originating from a severe storm off the Antarctic continent in the vicinity of (50°S, 5°E). In another work by O'Reilly et al. (1996), two buoys were deployed near (34.5°N, 120.7°W) during two periods: winter to early spring (mid-December 1992 to mid-May 1993), and late spring to summer (late May to mid-August 1993). Their observations showed that during the winter–spring period, the wave climate was dominated by North Pacific swells from a single-source region. During the late spring to summer months, however, the wave field was typically a mix of North and South Pacific swells with propagation angles differing by as much as 140°. Recently, Heimbach and Hasselmann (2000) reported the propagation of a huge swell from southeast of Tasmania (60°S, 145°E) toward the west coast of North America during June 1995. This event is seen as a northwest-to-southeast-oriented ridge on the ECMWF-based maps of significant wave height and mean wave frequency, as well as on the WAM- and ERS/SAR-based Hovmöller diagrams. Keeping in mind these systematic swell intrusions from the Southern Hemisphere, it is not surprising to see the resulting northward bending of the swell pools in boreal summer (Fig. 4b).

Besides this large-scale summer departure, several other features can also be identified in Fig. 4. Still in summer, the Afro-Asian monsoon-affected areas, notably the Arabian Sea, the South China Sea, as well as the waters surrounding Indonesia and north Australia, experience a significant weakening of swell influence. The Atlantic and Indian Ocean sectors of the Southern Ocean also exhibit a summer low in swell index. In contrast, weak swell areas shift completely in winter when they appear in the North Pacific and the northwest Atlantic (Fig. 4d). The swell pool in the Indian Ocean tends to extend southward in spring and westward in winter, while the size of it shrinks to a minimum in summer. It should be remembered, however, the swell and wind sea patterns revealed by this study are thought to be valid only for the open oceans. Given the spatial resolution of the present dataset (~100 km on average), some of the features in the marginal or enclosed seas, such as the Gulf of Mexico, might be unrealistic as a result of large-scale interpolation and smoothing.

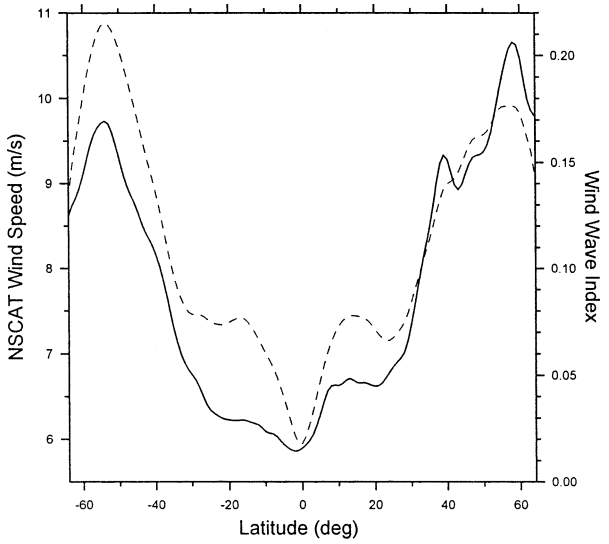

FIG. 5. Zonal distribution of the wind sea index (solid curve) derived from the collocated TOPEX/NSCAT and TOPEX/QSCAT datasets. Also overlaid is the simultaneous zonal wind speed climatology (dashed curve).

A systematic study on ocean wave spectrum using *ERS-1* synthetic aperture radar data was carried out by Heimbach et al. (1998), in which seasonal maps of swell wave height were produced. By comparing our Fig. 4 with their plate 4b one finds that they are substantially different in corresponding seasons. The fundamental difference is that the swell distributions in their results are, to a large extent, correlated to the seasonal variations of dominant wind belts; in contrast, the general swell pattern in our result has little similarity with that of the wind pattern. This obviously indicates the different effectiveness of the swell-wind sea classification schemes applied in the two studies.

4. Wind sea climate

a. Zonal distribution

The zonally averaged wind sea index (*W*, solid line) is shown together with wind speed (dashed line) in Fig. 5. The *W* distribution is characterized by a significant hemispheric asymmetry, with the Northern Hemisphere being much stronger than the Southern Hemisphere at corresponding latitudes, which may partly be ascribed to the asymmetrical distribution of the landmass between the two hemispheres. This is seen to be contrary to the zonal wind speed distribution (dashed line in Fig. 5) which displays a clear Southern Hemisphere dominance, especially in the extratropical areas. However, the two patterns in Fig. 5 do bear a resemblance, each reaching a minimum at the equator and increasing poleward until a maximum appears at about ±55° latitudes.

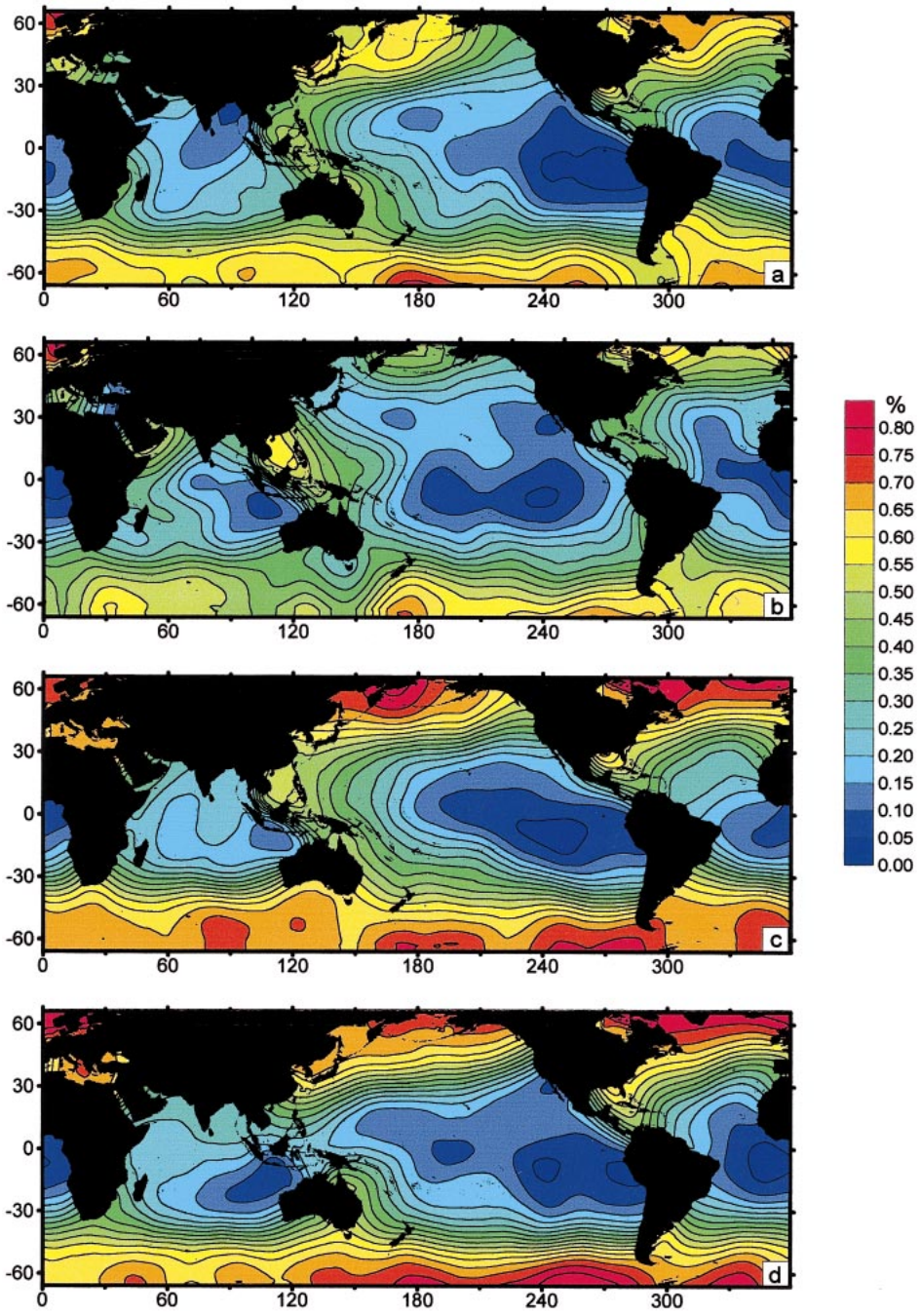

FIG. 6. Global distributions of the wind sea index for (a) spring (MAM), (b) summer (JJA), (c) autumn (SON), and (d) winter (DJF), derived from the collocated TOPEX/NSCAT and TOPEX/QSCAT datasets.

b. Seasonal variation

The seasonal maps of the wind sea index are presented in Fig. 6. Comparison with Fig. 4 shows that wave growth is generally weak in major swell pools. However, the opposite statement is not always true, that is, there is not necessarily strong wave generation in weak swell zones. In fact, areas of intense wave growth are observed in the northwest Pacific (including the Japan Sea and a large part of the China Seas), the northwest Atlantic, the Southern Ocean, and the Mediterranean Sea. Unlike swell, wind wave is directly related to local wind: the persistent westerlies in the Southern Hemisphere are responsible for the circumpolar wind sea belt in the Southern Ocean, while the extensive northwest gales from the main continents at midlatitudes during the winter half of the year are the primary cause of the

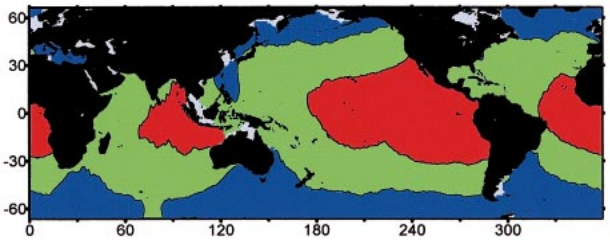

FIG. 7. Major swell pools (in red) and wind wave zones (in blue) of the world's oceans identified by using the *S* and *W* indices proposed in this study.

seasonal wind wave generation in the Northern Hemisphere. As an example, strong winds blowing constantly from Siberia toward the west coast of Japan can usually last for a period of longer than a day, and consequently generate numerous wind wave events in the Japan Sea (Ebuchi et al. 1992).

The seasonal variability of wind sea is found to be rather dramatic in the sense that a summer minimum (Fig. 6b) of its overall intensity is followed immediately by an autumn maximum (Fig. 6c). In winter, wind wave generation remains strong in the Northern Hemisphere while it weakens slowly in the Southern Hemisphere (Fig. 6d). With the onset of spring, both hemispheres exhibit a moderate wave growth (Fig. 6a). In addition to the general annual cycle, two regional features are noteworthy. The first is the antiseasonal enhancement of wind wave generation in the Arabian Sea and the South China Sea in boreal summer (Fig. 6b), which is obviously a consequence of the Asian monsoon. Note that during the same period, a broader area of the western Pacific and the western North Atlantic also displays an unusual wind sea pattern differing from other seasons (stretching poleward rather than equatorward, see Fig. 6b), which could be attributed, at least in part, to the fact that the frequency of tropical storms in those regions increases notably during summer and early autumn, and the trajectories of these storms appear to be largely poleward (Vitart et al. 1997). Another interesting feature is the wavelike structure appearing in the southeast coasts of Africa, Australia, and South America. This feature is visible throughout the year, though less obvious in summer. As far as we know, no previous study has explicitly mentioned such a feature. But there is a report on unusual wave activities along the Brazilian shoreline between 22° and 32°S resulting from a cyclone that developed over Uruguay in the lee of the Andes Mountains (Innocentini 1996). That study indicated the presence of a long-lived large fetch with surface wind velocities higher than 12 m s^{-1} directed toward the coast; some areas with velocities of 20 m s^{-1} were embedded in the fetch. If such strong fetches are common in those areas, the appearance of a wavelike pattern on the map of *W* index can then be expected.

The seasonal maps of the wind sea index (Fig. 6) are of more similarity in general pattern to their counterparts in plate 3b of Heimbach et al. (1998) compared to the case of swell. Note that the two results are based on satellite data of different years (1996–2001 for ours and 1993–95 for theirs), comparison of individual features may not make much sense. However, a systematic difference that can be identified is that the results of Heimbach et al. (1998) show a more distinct phase opposition in hemispheric wind sea climate compared to our results. This may be ascribed to the fact that their results are based on absolute wave height and our results are derived from a normalized wind sea index.

5. Summary

Knowledge on the global structure of swell and wind sea probabilities in a climatological sense is believed to be generally poor to date. This study represents the first of its kind toward a better understanding of these important parameters. It has benefited from the availability of simultaneous multisatellite missions, which provide independent measurements of wind speed and significant wave height with unprecedented accuracy. Using the two energy-based indices proposed in this study, the global distribution and seasonal variation of swell and wind sea climate of the ocean is investigated. As a summary, the identified major swell pools (in red) and wind wave zones (in blue) in the world's oceans are indicated in Fig. 7. Given the reasonable results obtained in this study and their general consistency with available field observations and model predictions, the proposed scheme appears to be effective and efficient in characterizing the global swell and wind sea climate. Further exploration based on this feasibility study with longer duration of collocation dataset (which can be readily achievable by incorporating simultaneous TOPEX/ERS measurements as well as other forthcoming concurrent altimeter/scatterometer missions) will undoubtedly lead to a more realistic and more complete description of the swell and wind sea conditions in the ocean, in particular, their interannual variabilities on a decadal timescale.

Acknowledgments. This work is cosponsored by the Natural Science Foundation of China (Project Numbers 40271083 and 40025615), the National High-Tech Project on Ocean Monitoring Technology (Numbers 818-AA63-03-06), and the Teaching and Research Award Program for Outstanding Young Teachers in Higher Education Institutions of MOE, PRC. The authors would like to thank Jerome Gourrion for his kind help in preparing the altimeter/scatterometer collocation datasets.

REFERENCES

Barber, B. F., and F. Ursell, 1948: The generation and propagation of ocean waves and swell. I. Wave periods and velocities. *Philos. Trans. Roy. Soc. London,* **240A,** 527–560.

Cartwright, D. E., J. S. Driver, and J. E. Tranter, 1977: Swell waves at Saint Helena related to distant storms. *Quart. J. Roy. Meteor. Soc.,* **103,** 655–683.

Chen, G., R. Ezraty, C. Fang, and L. Fang, 2002: A new look at the zonal pattern of the marine wind system from TOPEX measurements. *Remote Sens. Environ.*, **79,** 15–22.

Ebuchi, N., H. Kawamura, and Y. Toba, 1992: Growth of wind waves with fetch observed by the Geosat altimeter in the Japan Sea under winter monsoon. *J. Geophys. Res.*, **97,** 809–819.

Ewing, J. A., and A. K. Laing, 1987: Directional spectra of seas near full development. *J. Phys. Oceanogr.*, **17,** 1696–1706.

Forget, P., P. Broche, and F. Cuq, 1995: Principles of swell measurement by SAR with application to *ERS-1* observations off the Mauritanian coast. *Int. J. Remote Sens.*, **16,** 2403–2422.

Glazman, R. E., and S. H. Pilorz, 1990: Effects of sea maturity on satellite altimeter measurements. *J. Geophys. Res.*, **95,** 2857–2870.

Gourrion, J., D. Vandemark, S. Bailey, and B. Chapron, 2000: Satellite altimeter models for surface wind speed developed using ocean satellite crossovers. IFREMER Tech. Rep. IFREMER-DROOS-2000-02, 62 pp.

Groen, P., 1967: *The Waters of the Sea.* D. Van Nostrand Co., 328 pp.

Hamilton, G. D., 1992: Measurement of long-period, low-amplitude swell in the western North Atlantic Ocean. *J. Atmos. Oceanic Technol.*, **9,** 645–658.

Hasselmann, K., and Coauthors, 1973: Measurements of wind–wave growth and swell decay during the Joint North Sea Wave Project (JONSWAP). *Dtsch. Hydrogr. Z.*, **12,** 1–95.

Hasselmann, S., and Coauthors, 1988: The WAM model: A third generation ocean wave prediction model. *J. Phys. Oceanogr.*, **18,** 1775–1810.

Heimbach, P., and K. Hasselmann, 2000: Development and application of satellite retrievals of ocean wave spectra. *Satellite Oceanography and Society,* D. Halpern, Ed., Elsevier Oceanography Series, Vol. 63, Elsevier Science, 5–33.

——, S. Hasselmann, and K. Hasselmann, 1998: Statistical analysis and intercomparison of WAM model data with global *ERS-1* SAR wave mode spectral retrievals over 3 years. *J. Geophys. Res.*, **103,** 7931–7977.

Hwang, P. A., W. J. Teague, G. A. Jacobs, and D. W. Wang, 1998: A statistical comparison of wind speed, wave height, and wave period from satellite altimeters and ocean buoys in the Gulf of Mexico region. *J. Geophys. Res.*, **103,** 10 451–10 468.

Innocentini, V., 1996: A case study of the 9 August 1988 South Atlantic storm: Numerical simulations of the wave activity. *Wea. Forecasting,* **11,** 78–88.

Kahma, K., 1981: A study of the growth of the wave spectrum with fetch. *J. Phys. Oceanogr.*, **11,** 1503–1515.

Kinsman, B., 1965: *Wind Waves.* Prentice-Hall, 676 pp.

Lefevre, J. M., J. Barckicke, and Y. Ménard, 1994: A significant wave height dependent function for TOPEX/Poseidon wind speed retrieval. *J. Geophys. Res.,* **99,** 25 035–25 049.

Liang, N. K., 1990: A study of typhoon swell height prediction. *Acta Oceanogr. Taiwan,* **25,** 77–86.

Mettlach, T., D. Wang, and P. Wittmann, 1994: Analysis and prediction of ocean swell using instrumented buoys. *J. Atmos. Oceanic Technol.*, **11,** 506–524.

Mognard, N. M., 1984: Swell in the Pacific Ocean observed by SEASAT radar altimeter. *Mar. Geod.*, **8,** 183–210.

Munk, W. H., and F. E. Snodgrass, 1957: Measurements of southern swell at the Guadalupe Islands. *Deep-Sea Res.,* **4,** 272–286.

O'Reilly, W. C., T. H. C. Herbers, R. J. Seymour, and R. T. Guza, 1996: A comparison of directional buoy and fixed platform measurements of Pacific swell. *J. Atmos. Oceanic Technol.*, **13,** 231–238.

Pierson, W. J., 1991: Comment on ''Effects of sea maturity on satellite altimeter measurements'' by Roman E. Glazman and Stuart H. Pilorz. *J. Geophys. Res.*, **96,** 4973–4977.

——, and L. Moskowitz, 1964: A proposed spectral form for fully developed wind seas based on the similarity theory of S. A. Kitaigorodskii. *J. Geophys. Res.,* **69,** 5181–5190.

Queffeulou, P., B. Chapron, and A. Bentamy, 1999: Comparing Ku band NSCAT scatterometer and *ERS-2* altimeter winds. *IEEE Trans. Geosci. Remote Sens.,* **37,** 1662–1670.

Quilfen, Y., B. Chapron, A. Bentamy, and J. Gourrion, 1999: Global *ERS 1* and *2* and NSCAT observations: Upwind/crosswind and upwind/downwind measurements. *J. Geophys. Res.*, **104,** 11 459–11 469.

Snodgrass, F. E., G. W. Groves, K. Hasselmann, G. R. Miller, W. H. Munk, and W. H. Powers, 1966: Propagation of ocean swell across the Pacific. *Philos. Trans. Roy. Soc. London,* **249A,** 431–497.

Sverdrup, H. U., and W. H. Munk, 1947: Wind seas and swell: Theory of relations for forecasting. Publication 601, U.S. Navy Hydrographic Office, Washington, DC, 50 pp.

Vitart, F., J. L. Anderson, and W. F. Stern, 1997: Simulation of interannual variability of tropical storm frequency in an ensemble of GCM integrations. *J. Climate,* **10,** 745–760.

Young, I. R., 1999: Seasonal variability of the global ocean wind and wave climate. *Int. J. Climatol.*, **19,** 931–950.